

## Accepted Manuscript

Gold nanoparticles explore cells: Cellular uptake and their use as intracellular probes

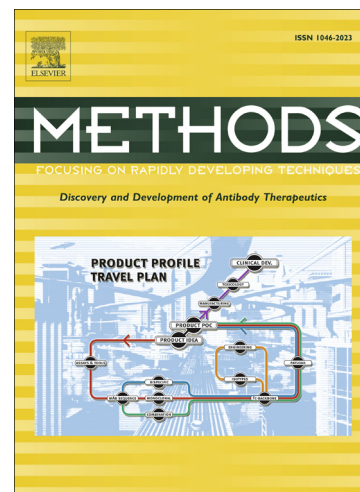
Anna Huefner, Dedy Septiadi, Bodo D. Wilts, Imran I. Patel, Wei-Li Kuan, Alexandra Fragniere, Roger A. Barker, Sumeet Mahajan

PII: S1046-2023(14)00036-X

DOI: <http://dx.doi.org/10.1016/j.ymeth.2014.02.006>

Reference: YMETH 3344

To appear in: *Methods*



Please cite this article as: A. Huefner, D. Septiadi, B.D. Wilts, I.I. Patel, W-L. Kuan, A. Fragniere, R.A. Barker, S. Mahajan, Gold nanoparticles explore cells: Cellular uptake and their use as intracellular probes, *Methods* (2014), doi: <http://dx.doi.org/10.1016/j.ymeth.2014.02.006>

This is a PDF file of an unedited manuscript that has been accepted for publication. As a service to our customers we are providing this early version of the manuscript. The manuscript will undergo copyediting, typesetting, and review of the resulting proof before it is published in its final form. Please note that during the production process errors may be discovered which could affect the content, and all legal disclaimers that apply to the journal pertain.

## Gold nanoparticles explore cells: Cellular uptake and their use as intracellular probes

*Anna Huefner<sup>1,5</sup>, Dedy Septiadi<sup>1,2</sup>, Bodo D. Wilts<sup>1</sup>, Imran I. Patel<sup>1,3,5</sup>, Wei-Li Kuan<sup>4</sup>,  
Alexandra Fragniere<sup>4</sup>, Roger A. Barker<sup>4</sup> and Sumeet Mahajan<sup>1,5</sup>*

<sup>1</sup>Sector for Biological and Soft Systems, Cavendish Laboratory, Department of Physics, University of Cambridge, 19 JJ Thomson Avenue, Cambridge, CB3 0HE, UK

<sup>2</sup>Institut de Science de d'Ingénierie Supremoléculaires, Université de Strasbourg, 8 Allée Gaspard Monge, 67083 Strasbourg Cedex, France

<sup>3</sup>Cancer Research UK Cambridge Institute, University of Cambridge, Li Ka Shing Centre, Robinson Way, Cambridge, CB2 0RE, UK

<sup>4</sup>John van Geest Centre for Brain Repair, University of Cambridge, Forvie Site, Robinson Way, Cambridge, CB20PY, UK

<sup>5</sup> Institute of Life Sciences and Department of Chemistry, University of Southampton, Highfield Campus, SO17 1BJ, Southampton, UK

### Abstract

Understanding uptake of nanomaterials by cells and their use for intracellular sensing is important for studying their interaction and toxicology as well as for obtaining new biological insight. Here, we investigate cellular uptake and intracellular dynamics of gold nanoparticles and demonstrate their use in reporting chemical information from the endocytotic pathway and cytoplasm. The intracellular gold nanoparticles serve as probes for surface-enhanced Raman spectroscopy (SERS) allowing for biochemical characterisation of their local environment. In particular, in this work we compare intracellular SERS using non-functionalised and functionalised nanoparticles in their ability to segregate different but closely related cell phenotypes. The results indicate that functionalised gold nanoparticles are more efficient in distinguishing between different types of cells. Our studies

pave the way for understanding the uptake of gold nanoparticles and their utilisation for SERS to give rise to a greater biochemical understanding in cell-based therapies.

### Keywords

Gold nanoparticles, nanoparticle uptake, intracellular imaging, surface-enhanced Raman spectroscopy, SERS

## 1. Introduction

Stem cells, understanding molecular mechanisms underlying the development of cancer and neurodegenerative diseases as well as studying the interactions of pathogens such as viruses and bacteria with cells are topical areas in molecular biomedical research. Though fluorescence microscopy is a major tool for cellular imaging, it has known limitations such as the invasiveness of the labelling (or staining) process, inability to monitor multiple molecular targets interactions as well as it suffers from photobleaching. Therefore, new imaging techniques and approaches that can identify molecules and interactions at sub-cellular resolution are very much required. One of the ways to achieve these objectives is to combine the use of nanoparticle-probes with intracellular molecular spectroscopy. Gold nanoparticles (AuNPs) can be used as probes and they have recently attracted a lot of attention in biomedical research due to their chemically inert nature and remarkable optical properties. AuNPs have been utilised in many applications such as biochemical sensing [1], drug and gene delivery [2, 3]. The rich optical properties of AuNPs arise from their ability to localise surface plasmons. This also enables their use as transducers for surface-enhanced Raman spectroscopy (SERS).

SERS is a highly sensitive, label-free, non-destructive and non-invasive method which allows for molecular identification giving it several advantages over other imaging techniques such as fluorescence, infrared, UV-visible or NMR [4-7]. In SERS, the otherwise extremely weak Raman scattering signal [8] is enhanced by several orders of magnitude by ensuring that the molecule is in very close vicinity of nanoparticles or of a nanostructured gold or silver surface [7, 9, 10]. The SERS spectrum is a vibrational 'fingerprint' which characterises the chemical bonds and symmetry of the molecule. [4] Recently, nanoparticle-based SERS has been employed in many biomedical applications from chemical sensing [11-13] to cancer detection in body fluids and tissues [14-17].

In contrast to conventional methods stated earlier, higher detection limits in addition to a complete structural characterisation of the target molecule can be achieved with SERS [18] without the need for staining or expressing fluorogenic proteins. It has also been demonstrated that SERS can be applied to living cells in order to monitor cellular functions [19], cell response to stress [20] and apoptosis [21]. SERS has been extensively applied in biomedical applications often for label-free detection of biomolecules in cells and tissues [4, 22]. AuNPs have been used as intracellular probes for SERS [23] to monitor release of drugs inside cells [24] as well as to probe molecules by targeting them to cellular compartments such as mitochondria, endosomes and the cell nucleus [11, 22, 25, 26]. The key for utilisation of nanoparticles inside cells for SERS and other measurements is their mechanism of uptake. Particle uptake has been achieved using physical methods such as microinjection [27, 28], electroporation [29], sonoporation [23, 30] and gene gun [31]. Further options for involuntary uptake are the translocation of particles through the plasma membrane facilitated by cell penetrating peptides (CPPs) [32, 33] such as the trans-activating transcriptional protein derived from viruses [34].

Moreover, AuNPs are known to be taken up by cells voluntarily whereby their intracellular uptake and distribution depends on many factors such as particle characteristics, e.g. charge, surface modification, particle size and shape [35-39] as well as experimental procedures involving

concentration and exposure time [40]. Different cellular mechanisms are involved in particle uptake such as phagocytosis and pinocytosis. The latter facilitates the uptake process through small membrane-bound vesicles, called endosomes.[41, 42] Pinocytosis can involve energy-dependent and receptor mediated endocytosis which has been shown to be the dominant internalisation pathway for several cell lines [36, 40, 43]. Following internalisation, membrane-bound vesicles encapsulating the particles mature and eventually fuse with lysosomes [41].

Hence, intracellular AuNPs are trapped inside membrane-bound vesicles of the endocytotic pathway [37]. Escape from these vesicles can only be achieved by functionalisation of the particle surface with peptides such as CPP [33, 34] and adenoviral receptor-mediated endocytosis peptides [44]. Trapped in endocytotic vesicles, particles get transported through cells via the common cellular transport mechanisms: by molecular motors such as myosin, kinesin and dynein along the intracellular filament network [45]. Studies have revealed various characteristics of these motor proteins *in vitro* and *in vivo* with reference to endocytotic organelles being transported. Friedman *et al.* measured the *in vivo* mobility of kinesin unattached to a surface using single molecule assays to be 600 to 800 nm/s [46-48]. Further studies revealed that average velocities strongly depend on the size of the attached cargo that is transported by these motors: a larger size appears to correlate with slower motions [49]. For example, 30 nm quantum-dots tagged to kinesin showed an average velocity of 600 nm/s in HeLa cells [49], whereas 1  $\mu\text{m}$  collagen-coated beads in murine embryonic fibroblasts displayed a velocity of  $\sim 10$  nm/s [50] and 3  $\mu\text{m}$  polystyrene beads in SV80 human fibroblasts showed similar velocities of 8 to 30 nm/s [51] suggesting that many factors influence the transport speed in cells. These factors include variations within the cell line, the bead size and its surface properties and material composition, which change the stall force of the motors and steric hindrance within the cell [50]. Moreover, the velocity of endocytotic vesicles such as endosomes in budding yeast and lysosomes in African green monkey kidney cells was tracked and gave values of  $(213 \pm 139)$  nm/s [52] and  $\sim 410$  to 450 nm/s [53], respectively.

In this work, we probe cellular uptake and dynamics of AuNPs optically. The particle uptake is studied with non-functionalised (citrate-capped) AuNPs revealing different trajectories and speeds which correlate with different transport and diffusion mechanisms inside cells. Such internalised AuNPs serve as intracellular SERS probes. We use these nanoparticle-probes taken up through the endocytotic uptake pathway to report SERS and utilise this information to evaluate their ability to segregate different cell phenotypes. Further we also employed AuNPs functionalised with nuclear localisation signal peptide (NLS) as SERS probes. The functionalised nanoparticle-probes give much better cellular phenotype distinction compared to non-functionalised AuNPs. This work reaffirms the nanoparticle-probe based SERS methodology for intracellular investigations and for achieving cellular distinction.

## 2. Methodology

### 2.1 Cellular uptake and dynamics of AuNPs inside cells

All experiments were carried out on undifferentiated (UDC) and differentiated (DC) SH-SY5Y cells, a human neuroblastoma cell line, cultured and maintained as described elsewhere [26]. Both cell phenotypes are adherent and display a flat and neuronal morphology. Fluorescence staining with Hoechst 33343 (Invitrogen, UK) and anti-dopamine antibody (Anti-DA) (mouse, 1/1000, Millipore, UK) were carried out according to staining procedures described elsewhere [26, 54]. Cells were grown in collagen-coated glass bottom dishes (MatTek, US) and incubated with citrate-capped spherical AuNPs (BBInternational, UK) of different diameters (40 nm, 60 nm, 100 nm) at a concentration of 200,000 particles per cell independent of particle size illustrated in Fig. 1A. The

uptake of particles is shown for an incubation time of 24 and 48 hours in Fig. 1B-D for 40 nm, 60 nm and 100 nm particles. Based on these images, internalisation of particles is visible. We could observe aggregates of nanoparticles inside cells, which appear as dark spots. No aggregation of AuNPs is observed in the cell culture medium (**see Supporting Information**) and therefore we believe that aggregation is induced inside the endocytotic compartments. There is no indication that non-functionalised, intracellular AuNPs are localised outside the endocytotic pathway as also observed using transmission electron microscopy by Tkachenko *et al.* [37]. In the images shown in Fig. 1B-D, some nanoparticles can be seen outside cells. These are immobile aggregates which stick to the coating of the cell culture dishes.

In order to track and characterise the motion of particles or intracellular vesicles, they have to be imaged in a time-dependent way that allows extraction of important biophysical parameters like speed of the particle and the diffusion constant. This is commonly performed by measuring the mean-square displacement (MSD) of a particle within a given lag time  $\Delta t$ . It is calculated in two dimensions as follows:

$$MSD(\Delta t) = \langle (\Delta r(\Delta t))^2 \rangle = \langle (x(t) - x(t + \Delta t))^2 + (y(t) - y(t + \Delta t))^2 \rangle. \quad (1)$$

The resulting trajectories can be classified into models describing different types of motions such as anomalous subdiffusion or confined random walk

$$MSD(\Delta t) = 4D\Delta t^\alpha \quad (2)$$

and directed motion as superposition of diffusion and transport

$$MSD(\Delta t) = 4D\Delta t + (v\Delta t)^2. \quad (3)$$

While based on the Einstein-Stokes relation, the diffusion constant  $D$  for spherical particles subject to Brownian motion in two dimensions can be described as

$$D = k_B T / (4\pi\eta r) \quad (4)$$

where  $k_B$  is the Boltzmann's constant,  $T$  is the absolute temperature,  $r$  is the particle radius and  $\eta$  is the fluid shear viscosity.

For tracking nanoparticles, bright field images of live cells were obtained in trans-illumination using a 40x condenser (NA=0.6) and a 100x oil immersion (NA=1.4) objective with a white light source on a confocal microscope system (Leica, Germany). Images were captured using the Leica microscope software, Leica LAS AF Lite. We recorded time lapse videos of DCs incubated with 100 nm AuNPs for 72 hours with 120 to 180 frames and frame rate of 1 frame/s.

Image analysis was performed using *ImageJ* software (Rasband, W.S., ImageJ, U. S. National Institutes of Health, Bethesda, Maryland, USA, <http://imagej.nih.gov/ij/>, 1997-2012) [55]. The colour threshold of single images was modified manually to allow accurate recognition of particles inside cells for later analysis. In order to estimate cellular particle uptake with relevance to later SERS measurements, the number of nanoparticles was determined by calculating the surface area of cells occupied by nanoparticles divided by the surface area  $A$  of a single nanoparticle ( $A = \pi r^2$ ). 20 cells per sample group were analysed.

In order to characterise the motility of intracellular AuNPs, nanoparticle tracking was performed by using *speckletrackerj*, an additional plugin for *ImageJ* software (developed by Athena's group, Lehigh University, US) [56]. AuNPs were tracked for particles which appeared as diffraction limited spots or larger.

## 2.2 SERS studies with intracellular AuNPs

### 2.2.1 Sample preparation

For AuNP-based SERS on UDCs and DCs, cells were grown on 13 mm, poly-L-lysine (Sigma-Aldrich, UK) coated glass cover slips (Agar Scientific, UK). As indicated in Fig. 1E, cellular particle uptake varies with particle size. In order to make the two different particle sizes comparable, volume equivalence for the particles was chosen. Hence, 40 nm AuNPs were incubated at 675,000 particles per cell while 60 nm AuNPs were incubated at a concentration of 200,000 particles per cell in a multi-well plate (see scheme 1A). Each well was seeded with approximately 50,000 cells. Previously, we have shown using UV-visible spectra (**also see Supporting Information**) that under these experimental conditions, AuNPs remain dispersed as a colloid in solution [26] which might be due to the formation of a protein corona around the NPs in cell culture medium [57]. A small fraction of AuNPs adhere to the poly-L-lysine coating of the cell culture dish forming small, immobile aggregates. In order to increase the cellular nanoparticle uptake, an incubation time of up to 72 hours was used. The cellular uptake efficiency did not pose a limiting factor for SERS measurements in our experiments. We have also shown earlier that the cells remain viable under these incubation conditions and the methodology in this paper is primarily based on our earlier paper [26]. Thereafter, cells were washed twice in cell culture medium in order to remove particles not taken up. After washing twice with phosphate buffered saline, cells were incubated in 4% formaldehyde for 10 minutes for fixation and afterwards kept in phosphate buffered saline for SERS measurements.

AuNPs functionalised with the nuclear localisation signal peptide (CGTG-PKKRKV-GGK-(Flu)peptide sequence, PeptideSynthetics, Fareham, UK) were incubated with UDCs as well as DCs. 375  $\mu\text{l}$  of 40 nm AuNPs reagent ( $9 \times 10^{10}$  particles/ml) or 385  $\mu\text{l}$  of 60 nm AuNPs reagent ( $2.6 \times 10^{10}$  particles/ml, both BBInternational, UK) were conjugated with NLS in a concentration NLS:AuNP of 100:1 as described earlier [26].

### 2.2.2 Acquisition, processing and analysis of SERS data

A Renishaw® inVia Raman microscope with a 633 nm laser in streamline mode and a Leica 100x (NA=0.85) objective in combination with Wire3.3 software was used to acquire spectral SERS data sets of whole cells (one cell per data set). Generated maps have a pixel size of 600 nm x 600 nm. The collection time per line of spectra was 20 s over a spectral range from 400 to 2200  $\text{cm}^{-1}$ . The excitation intensity was approximately  $2 \times 10^4 \text{ W/cm}^2$ .

Spectral data was pre-processed using MATLAB R2010b employing custom-made procedures for removal of the SERS background and data set reduction as described earlier [26]. Following data pre-processing, data analysis was carried out as a combination of principal component analysis (PCA) and linear discriminant analysis (LDA) using MATLAB R2010b with IRootLab (<https://code.google.com/p/irootlab/>), a graphical user interface toolbox for vibrational biospectroscopy data analysis [58, 59]. As Martin *et al.* have described, PCA is a common technique to classify biological sample groups [59]. PCA, an unsupervised, multivariate data reduction technique, has previously been used in context with SERS imaging [20], e.g. to achieve high diagnostic sensitivity in cancer detection [16]. Generated SERS spectral maps require a powerful analysis method to reduce its dimensionality and recognise a common pattern such as by using PCA. It generates principle component (PC) loadings and PC scores from the initial or pre-processed data. The original data and PC scores are correlated by the PC loading, which is similar to a correlation coefficient. PC loadings identify features (i.e., peak in a SERS spectrum) with highest importance within the data. Therefore, PC1 loadings plots allow for characterisation of the spectral variation within the data set. As PCA describes similar patterns which correlate to the data, these are not necessarily those which allow for ultimate data set distinction. Therefore, a method is required which finds differences within data sets. LDA is a supervised method for group classification. It seeks

for  $n-1$  projections of  $n$  data sets that allow for complete separation of those groups. LDA by itself does not facilitate data reduction. [60] Therefore, a two-stage feature extraction method (i.e. PCA-LDA) is required to allow for data reduction and classification.

In our study, individual, pre-processed data sets (150 single spectra per data set) were mean-centred and PCA was applied. Spectral, normalised PC1 loadings plots were used to characterise and compare sample groups. In order to allow for group classification, PCA-LDA was applied on mean-centred, vector-normalised individual data sets and LD1 scores vs. LD2 scores were plotted with data point colouration according to cell groups. Further characterisation of LD scores distributions was done using 1D intensity curves. They were generated employing Kernel density estimation (bandwidth = 1000) to smooth LD scores histograms (with bin size = 50) and normalised.

### 3. Results and discussion

#### 3.1 Size-dependent cellular uptake

Results from cellular uptake of nanoparticles of different sizes are shown in Fig. 1E for differentiated cells (DCs). We observed an increment in the number of AuNPs taken up with increased incubation time from 24 hours to 48 hours independent of particle size. Fig. 1E indicates an increase of 90% in cellular uptake of 40 nm and 51% increase for 60nm AuNPs, during the subsequent 24 hours of incubation. An increase in size of the nanoparticles leads to an increment in the number of AuNPs taken up which is in accordance with other studies [30, 61-63]. These results reveal that cellular uptake is dependent on size and incubation time.

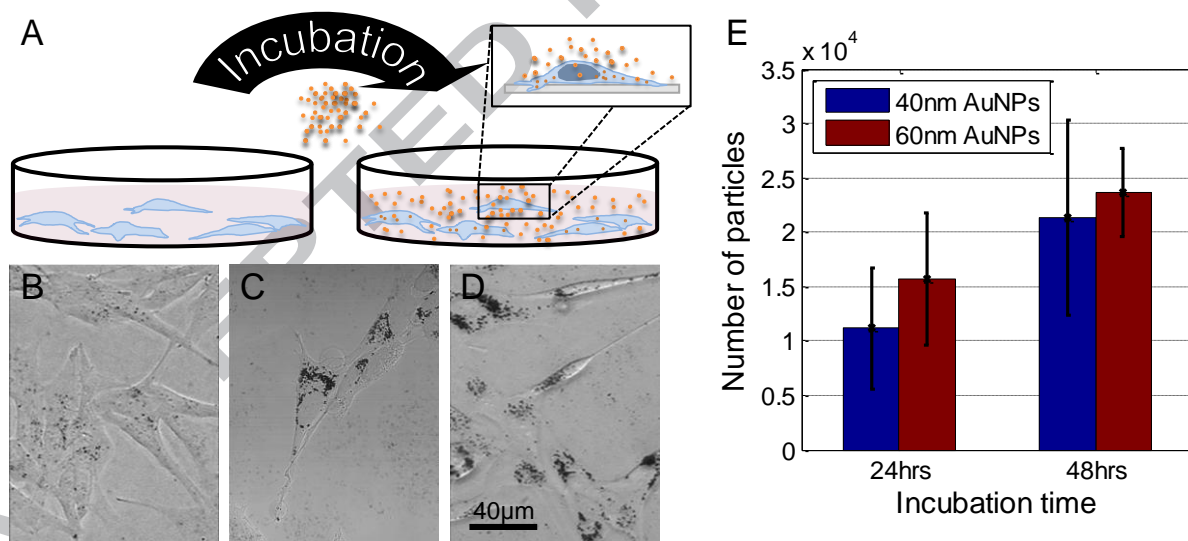


Figure 1: Schematic of methodology (A) and images showing cellular uptake of 40 nm (B), 60 nm (C) and 100 nm (D) AuNPs after 48 hours of incubation in differentiated SH-SY5Y cells. E) The uptake of 40 nm (blue bars) and 60 nm (red bars) AuNPs into differentiated SH-SY5Y cells ( $n=20$  for each group) was determined by processing optical images.

#### 3.2 Motility of intracellular AuNPs

Following intracellular uptake through endocytosis, all intracellular nanoparticles are localised in endocytotic vesicles such as endosomes and lysosomes. These vesicles are known to be transported through the cell via molecular motors [64]. Usually, bright field images do not reveal the localisation and motility of endocytotic vesicles within a cell due to almost negligible optical contrast compared

to the surrounding cellular structures. As AuNPs used for our studies are taken up through the endocytotic pathway, they serve as a 'stain' for visualising endocytotic vesicles. Particulates and aggregates of different sizes are seen inside cells as shown in Fig. 2A. Tracking their movement (as described in 2.1) reveals different types of motions which give information about cellular characteristics such as the viscosity/diffusion constant inside endocytotic vesicles and transport velocity. For understanding this we employed particle tracking analysis to see the movement of AuNPs aggregates inside and outside SH-SY5Y cells. Using particle tracking software as described in 2.1, 150 particle aggregates were randomly selected from time-lapse videos of DCs. As cells were incubated with 100 nm AuNPs for 72 hours, endocytotic vesicles appear to have a round shape and are packed with AuNPs (Fig. 2A). Particle aggregates used for tracking followed a size distribution as shown in Fig. 2B with an average radius of  $(464\pm 64)$  nm. The rather larger size of vesicles is advantageous for tracking its motion as vesicles that were slightly out of focus were still detectable. Detected tracks refer to the centre point of the particle aggregates.

The *MSD* was calculated according to Eq. 1 using MATLAB R2010b. Fig. 2 shows typical traces and *MSD* for the four different motions that were observed. Fig. 2C-F show the displacements in two dimensions (**also see Supporting Information for results plotted with the same x and y-axis scale**) and Fig. 2G-J show the appropriate *MSD* vs.  $\Delta t$  plots. It is pointed out that our 2-D analysis would underestimate the velocities compared to a full (3D) vectorial analysis. However, due to the relatively flat cells (neuronal cells) used in the study; the z-movement is likely to be minimal. In any case the general description and analytical principles would still be valid with our 2-D analysis. The *MSD* vs.  $\Delta t$  plots allow for easy categorisation of different motions. Fig. 2C and 2G show an example for an isotropic random walk. Fitting Eq. 2 to the *MSD* vs.  $\Delta t$  plot in Fig. 2G reveals a diffusion constant,  $D_{diffusion} = (0.70\pm 0.15) \mu\text{m}^2/\text{s}$  of the particle aggregate inside an endocytotic vesicle within the cytoplasm as well as the time exponent,  $\alpha = 1.03\pm 0.06$ .  $\alpha \approx 1$  in Eq. 2 implies that this motion corresponds to Brownian motion of particulates inside cells. An example of a partially confined random walk is shown in Fig. 2D and 2H. This motion is characterised by alternating regions of almost linearly increasing *MSD* and plateaus indicating that the movement changes from random walk to confined motion. An oscillating *MSD* over  $\Delta t$  as visible in Fig. 2I is characteristic for an oscillating motion as confirmed by the track in Fig. 2E. This motion suggests the adsorption of particles to the membrane inside vesicles as also described by Jin *et al.* [65]. Fig. 2F represents a confined motion/transport of a vesicle within the cell superposing the diffusion of the vesicle within the cytoplasm. Typical trajectories follow non-uniform linear motions; their *MSD* over  $\Delta t$  (Fig. 2J) increases quadratically as described by Eq. 3. Fitting Eq. 3 (red line in Fig. 2H) reveals an exemplary transport velocity of  $v_{transport} = (39\pm 4)$  nm and a cytoplasmic diffusion constant during active transport of  $D_{transport} = (6.6\pm 0.6)\cdot 10^{-3} \mu\text{m}^2/\text{s}$ . The contribution of active transport is much higher than that of free diffusion which suggests a binding of the vesicle to the cytoskeletal filament network *via* molecular motors. Values for the diffusion constant and the vesicle velocity are in agreement with results from Levi *et al.* [50] and Caspi *et al.* [51].

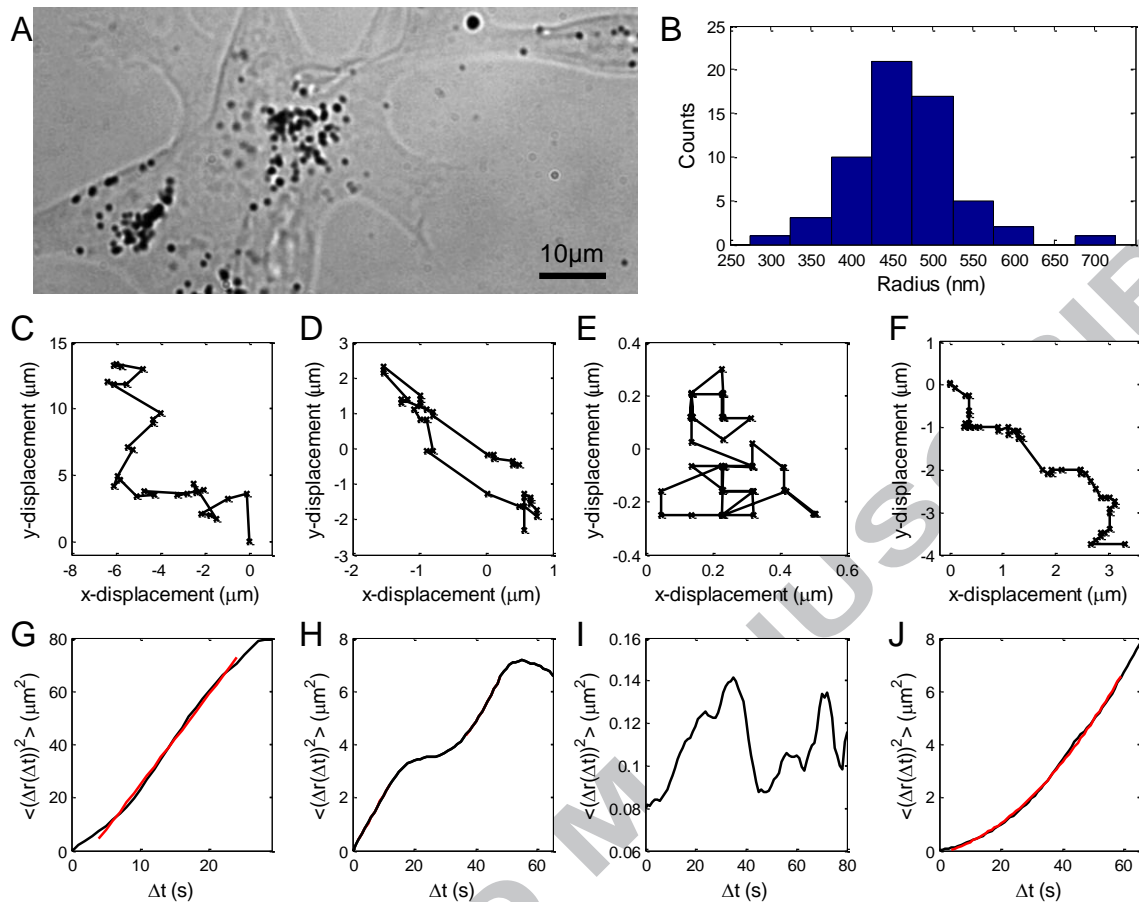


Figure 2: A) The bright field image shows intracellular nanoparticle aggregates after 72 hours of incubation. Those aggregates used for motility tracking showed an average radius of  $(464 \pm 64)$  nm (B). Tracking analysis revealed different types of motions, where (C-F) show the trajectories and (G-J) the corresponding  $MSD$  vs.  $\Delta t$  plots. The following motions are examples of motions commonly observed: random walk of particle aggregate inside vesicle (C, G), partially confined random walk (D, H), oscillation of particles due to confinement to membranes (E, I), transport process/confined motion (F, J). Red lines (G, J) are fittings to the  $MSD$  plots revealing the diffusion constant inside vesicles to be  $D_{diffusion} = (0.70 \pm 0.15) \mu m^2/s$  (G) and the typical transport velocity  $v_{transport} = (39 \pm 4) nm/s$  (J). Plots in C-F have different scales to highlight the particle trajectories. For plots with a uniform x-scale see Fig. S2 in the supporting information.

Generally, the track of one particle shows intervals of different types of motions impeding a clear distinction between them. Just a few tracks exclusively show only linear motion or active transport. To translate findings from Fig. 2J to an average transport velocity, motion tracks ( $n=23$ ) showing active transport have been chosen as summarised in the  $MSD-\Delta t$  log-log plot in Fig. 3A. The running average of  $MSD$  was calculated according to Eq. 1, followed by calculating the diffusion constant  $D=MSD/(4\Delta t)$ , where  $\Delta t$  was chosen to be smaller than a quarter of the total number of data points [50]. This common methodology is based on the unbiased assumption that the dominant motion (active transport over diffusion) contributes the most to the overall motion of the particle. The histogram of  $-\log D$  is presented in Fig. 3B showing a double peak Gaussian distribution. A multi peak fit (red line) reveals the peak positions as  $0.20 \pm 0.03$  and  $1.92 \pm 0.05$  equivalent to diffusion constants of  $D_1 \approx 0.6 \cdot 10^{-1} \mu m^2/s$  and  $D_2 \approx 10^{-2} \mu m^2/s$ , respectively. The smaller distribution around  $D_1$  corresponds to the diffusion constant of AuNP aggregates themselves inside endocytotic vesicles in the cytoplasm. The second, much higher distribution around  $D_2$  corresponds to the diffusion constant of AuNP aggregates inside endocytotic vesicles while actively transported by molecular motors attached to the filament network of the cytoskeleton. This explains why  $D_1$  is larger than  $D_2$ .

This double distribution is indicative of the diffusion constant for active transport as well as for diffusion inside the intracellular environment and has been described before in particle tracking experiments with quantum dot-conjugated prion proteins inside yeast cells by Tsuji *et al.* [66]. Furthermore, Fig. 3C summarises the velocity distribution of active transport, showing a dominant peak at  $(36\pm 2)$  nm/s followed by two minor peaks at  $(182\pm 24)$  nm/s and at  $(251\pm 39)$  nm/s determined by local Gaussian fits (data not shown). This indicates that active transport with a velocity of  $\sim 30$  to  $40$  nm/s is the dominant process, but faster motions could also be observed with values comparable to velocities of endocytic traffic observed by Toshima *et al.* [52]. Aggregates of AuNPs as tracked in our study show a higher density and average sizes that are in excess compared to those used in other studies [46-49]. This can result in increased steric hindrance during active transport in addition to an increased load ratio on the molecular motors that ultimately causes their motion to be slowed down as been shown by Coppin *et al.* [67]. They observed the slow-down and final stall of kinesin motors under opposing loads of 5 pN together with dissociating of kinesin motors from microtubules.

In order to actively move aggregates of AuNPs through a medium/cell, the pulling force has to exceed the drag force  $F=6\pi\eta rv$  ( $r$  is the radius of the spherical particle and  $v$  its velocity,  $\eta$  is the dynamic viscosity) under the idealised assumption of hydrodynamic regime for the friction and under idealised geometries. Eq. 4 connects the diffusion  $D$  with the viscosity  $\eta$  resulting in the required drag force  $F=vk_B T/D$  with  $k_B$  is the Boltzmann's constant and  $T$  the temperature. Using our experimental results  $v_{transport}$  and  $D_{transport}$  of active transport as calculated in Fig. 2J reveals a required drag force of 0.1 pN. As estimated under idealised conditions, the required drag force for actively transported AuNP aggregates with a size of  $\sim 1$   $\mu\text{m}$  might under real conditions eventually reach the range of described stall forces connected with a slow-down of transport motions as observed by Coppin *et al.* [67].

Following the tracking of AuNPs inside and outside cells, the motility of actively transported particles was characterised further (Fig. 3A-C). Trajectories of all 150 tracked AuNP aggregates are summarised in a  $-\log D$  plot in Fig. 3D. Multiple Gaussian peaks were fitted to the distribution which reveal a shoulder at  $-0.46\pm 0.10$  as well as peaks at  $0.48\pm 0.03$  and  $1.70\pm 0.07$  corresponding to  $D$  values of  $\sim 10^1 \mu\text{m}^2/\text{s}$ ,  $\sim 10^{-1} \mu\text{m}^2/\text{s}$  and  $\sim 10^{-2} \mu\text{m}^2/\text{s}$ , respectively. These diffusion constants represent different conditions. The first  $D$  value represents AuNP aggregates diffusing outside the cell indicated by the high diffusion constant. This has been described in particle tracking experiments in biological buffers in other studies before [66]. The latter values are related to active transport corresponding to diffusion inside endocytotic vesicles and active transport whilst being attached to molecular motors. Furthermore, we observed outliers for  $3 < -\log D < 4$  corresponding to  $D \sim 10^{-4} - 10^{-3} \mu\text{m}^2/\text{s}$ . Such a low diffusion constants are characteristic to oscillating motions (Fig. 2E and 2I) corresponding to particles being confined to membranes.

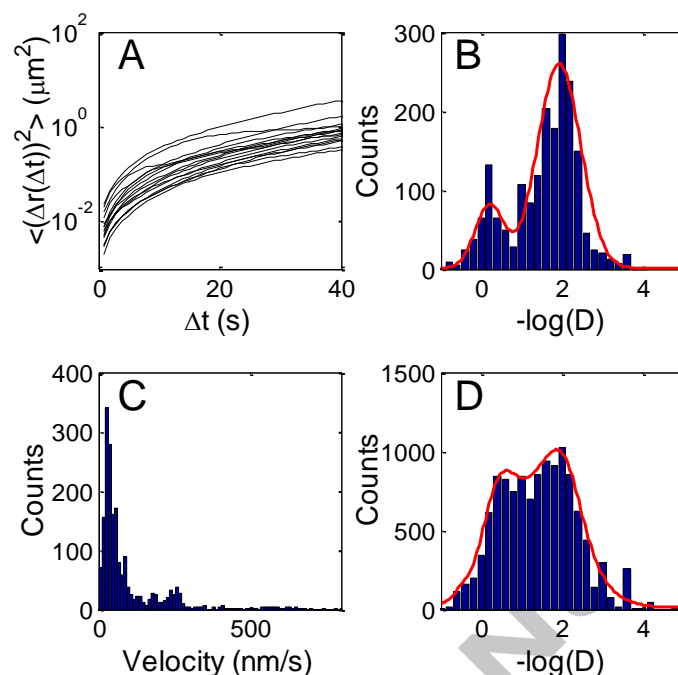


Figure 3: Particle aggregates following linear tracks ( $n=23$ ) were chosen and  $MSD$  vs.  $\Delta t$  (A),  $-\log D$  histogram (B) as well as the velocity distribution (C) are plotted. 150 vesicles were tracked over time intervals between 40 and 180s.  $MSD$  was calculated for  $\Delta t=10$ s for each track shown in a  $-\log D$  histogram (C) with multiple Gaussian peaks (red line) fitted to the distribution with a shoulder at  $(-0.46\pm 0.10)$ , peaking at  $(0.48\pm 0.03)$  and  $(1.70\pm 0.07)$  as well as outlier for  $3 < -\log D < 4$ . They represent the diffusivity of particles free in the cell culture medium ( $D \sim 10^0-10^1 \mu\text{m}^2/\text{s}$ ), diffusivity inside cellular organelles of the endocytotic pathway ( $D \sim 10^{-1} \mu\text{m}^2/\text{s}$ ), diffusivity during active transport ( $D \sim 10^{-2} \mu\text{m}^2/\text{s}$ ), as well as oscillating motion ( $D \sim 10^{-4}-10^{-3} \mu\text{m}^2/\text{s}$ ).

In summary, particle tracking used for studying the motility of particle aggregates helped in understanding the location (inside or outside cell using diffusion coefficient) and behaviour (e.g. aggregation inside intracellular, endocytotic vesicles) of intracellular AuNPs. Knowing these characteristics in combination with quantitative estimations of particle uptake (as investigated in 3.1) demonstrate that AuNPs are suitable intracellular probes for techniques taking advantage of particle uptake. SERS exploits these properties ideally as it uses intracellular aggregates of AuNPs as nanoantennas to report their local chemical environment. Our results exploiting the natural uptake of AuNPs to act as intracellular SERS probes are detailed below.

### 3.3 Cellular imaging using SERS

While incubation of cells with AuNPs, particles are gradually taken up through the endocytotic pathway inside the cell. Intracellular AuNPs are likely to form aggregates inside of endosomes/lysosomes. Exemplarily this is shown for an undifferentiated cell (UDC) incubated with 40 nm AuNPs for 72 hours in Fig. 4A. While AuNP aggregates of different sizes are distributed all over the cell the nuclear region, highlighted by a white ellipse, is clearly omitted. Intense SERS signals could only be achieved from those areas showing aggregates.

Raman scanning measurements gave a spectrum for every pixel interrogated within the field of interest, usually, in our case, a single cell. The intensity of single peaks or peak regions, assigned to a

particular molecular vibration(s), within the field of interest can be used to generate pseudo-colour maps representing their distribution within the sample. This allows for tracking several different molecules, i.e. proteins or lipids, located in the close vicinity of our ‘nanoparticle-probes’ after a single scan of the sample without the need for molecule-specific stains and/or markers. This makes SERS hugely advantageous over other molecular imaging techniques. Fig 4B-C shows the molecular distribution of proteins (Fig. 4B) and lipids (Fig. 4C) of the sample cell shown in Fig. 4A. Characteristic peptide and protein bands in SERS are amide I ( $1600 - 1700 \text{ cm}^{-1}$ ) and amide III ( $1200 - 1400 \text{ cm}^{-1}$ ) bands. Furthermore, lipids show characteristic SERS peaks at  $1116 \text{ cm}^{-1}$  (C-C stretch),  $1260 \text{ cm}^{-1}$  (C-H stretch),  $1300 \text{ cm}^{-1}$  (C-H<sub>2</sub> twist) and  $1440 \text{ cm}^{-1}$  (C-H<sub>2</sub> bend). [68] Exemplary SERS spectra from the maps generated in Fig. 4B-C are presented in Fig. 4D showing some of the mentioned protein and lipid peaks. Its high molecular resolution makes SERS a suitable method for sensing biomolecular changes. In this context, we demonstrate that intracellular nanoparticles-based SERS allows the distinction of closely related cell (pheno)types which differ in their biochemical makeup.

### 3.4 Intracellular SERS imaging with non-functionalised AuNPs

The use of optical and fluorescence microscopy has led to many developments in identification of cellular structures. However, due to the lack of chemical distinction ability, non-invasive and label-free classification of closely related cell phenotypes remains one of the big challenges. We first employed bare 40 nm AuNPs voluntarily internalised by cells through the endocytotic pathway as intracellular SERS nanosensors in UDCs ( $n=12$ ) and DCs ( $n=26$ ); closely related neuronal cells showing similar morphologies [69]. These citrate capped (non-functionalised) nanoparticle-probes (also see 3.1 and 3.2) are taken up entirely through the endocytotic pathway. Hence, these SERS nanoparticle-probes should sense the ingredients of this cellular ‘digestive system’ of the cell.

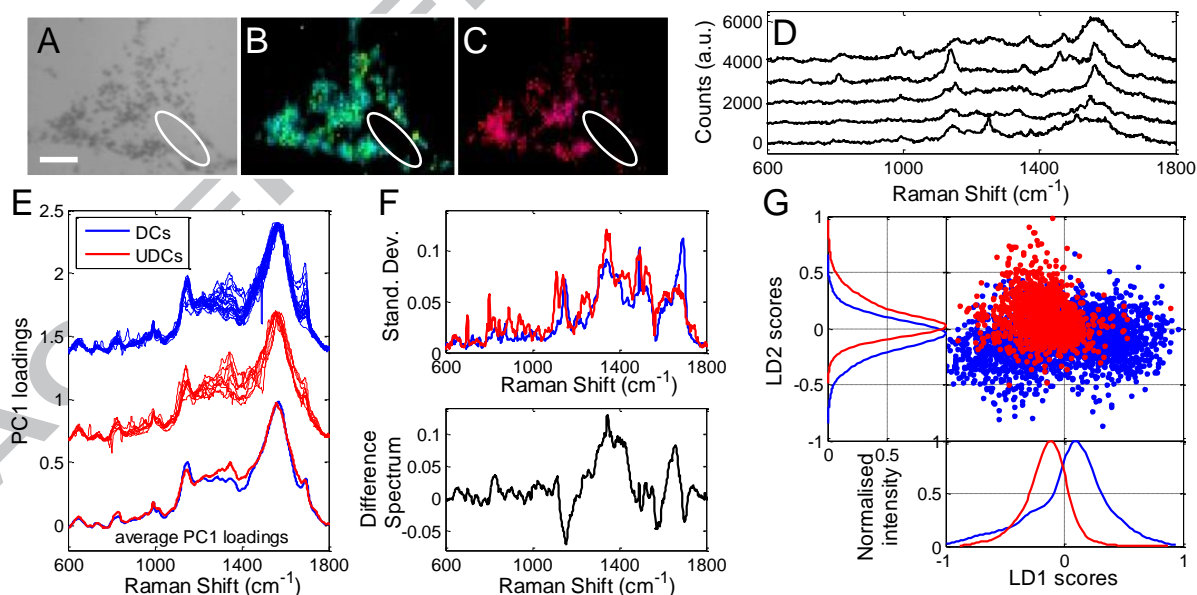


Figure 4: A) Bright field image of a UDC after 72 hours of incubation with 40 nm AuNPs showing many intracellular particle aggregates outside the cell nucleus as highlighted with a white ellipse (scale bar: 10  $\mu\text{m}$ ). Corresponding SERS maps (B-C) revealing the intracellular distribution of proteins (B, green: C-C/C-N stretch, yellow: C-H deformation, cyan: C-H<sub>3</sub> deformation) and lipids (C, magenta: C-H<sub>2</sub> twist, red: C=C stretch). The SERS images were generated by scanning with a pixel size of 600 nm x 600 nm. D) Five, background subtracted spectra (D) from different intracellular positions exemplary illustrate the molecular variance recorded by our ‘nanoantennas’ inside cells. E-F) Principal component loadings of single cell SERS data sets from UDCs (red) and DCs (blue) incubated

with non-functionalised 40 nm AuNPs for up to 72 hours. Single cell PC1 loadings (E) as well as cell group average (bottom, E), standard deviation (top, F) and the difference spectrum of the cell group averages of UDCs and DCs (bottom, F) show that differences in the average PC1 loadings of cell groups are rather caused by divergences within the cell group. G) PCA-LDA revealing LD1 vs. LD2 scatter plot with corresponding 1D intensity plots alongside. Even though LD scores show overlap between the cell groups, the LD1 scores intensity curve of UDCs (red) and DCs (blue) shows clear distinction due to its shape.

Single cell SERS maps were acquired from cells of each cell group (UDCs and DCs), data sets pre-processed (see 2.2.2) and PCA was performed. In Fig. 4E resulting PC1 loadings for all UDCs (red lines, middle) and DCs (blue lines, top) as well as their average loadings (bottom) are shown. Comparing PC1 loadings of both cell groups, small differences between the cell group average loadings can be seen in the range of 1100 - 1750  $\text{cm}^{-1}$ . In order to evaluate if these differences between the average loadings are caused by general divergence within samples of the same group or between the cell groups, corresponding standard deviations (STD) within all PC1 loadings of each cell group (top spectrum in Fig. 4F) as well as the difference spectrum of the average PC1 loadings of UDCs and DCs (bottom) are given in Fig. 4F. The STD of single PC1 loadings between 1100 and 1750  $\text{cm}^{-1}$  partly show values above 5%. In particular, between 1100 - 1200  $\text{cm}^{-1}$  (STD of 8%) and within the amide I band (i.e. 1300 - 1380  $\text{cm}^{-1}$ , 1470 - 1510  $\text{cm}^{-1}$  and 1675 - 1710  $\text{cm}^{-1}$ ) the STD increases up to 12%. Therefore, the difference spectrum in Fig. 4F (bottom) rather appears to be subject to the variance of data sets within one cell group than the variance within the both cell groups. In this case PCA by itself did not allow for cell group segregation, hence, PCA-LDA was applied and the resulting LD1 vs. LD2 scores 2D scatter plot is shown in Fig. 4G. Corresponding 1D intensity plots (see 2.2.2) of the LD1 and LD2 score distributions are shown alongside for UDCs (red) and DCs (blue). As expected from PCA results, the scatter plot shows a significant overlap between both cell groups. Only the 1D intensity curves reveal more detailed characteristics of the data point distribution. For UDCs, the LD1 scores intensity distribution is Gaussian and peaks at -0.12. The LD1 scores distribution of DCs peaks at 0.09 and has a shoulder at around -0.04. LD2 scores distributions are Gaussian peaking at 0.22 and -0.4 for UDCs and DCs, respectively. These results in combination with the PC1 loadings confirm great similarities between the cell groups. In particular, the distribution of LD2 scores of both cell groups are very close together. Also, LD1 scores of UDCs overlap broadly with those of DCs for values  $<0$ . Nevertheless, PCA-LDA revealed that slight differences are also present. The LD1 scores double-peak distribution of DCs has one peak/shoulder completely overlapping with UDCs, but also shows a peak separated from the other cell group, indicating that some molecular features are only present in DCs. Cellular differentiation in SH-SY5Y cells was induced using staurosporine, an inhibitor of various protein kinases [70, 71]. Staurosporine initially causes a change of the cellular metabolism as observed by Deshmukh *et al.* [72] even though exact mechanisms involved are not known yet [70, 71]. These metabolic changes on the one hand drive the differentiation process [73, 74] and on the other hand cause shifts between cellular glycolysis and oxidative phosphorylation due to modified cellular metabolite level and redox state [75]. These intracellular developments might cause the cellular uptake needs of the cell to change slightly which we were able to detect using AuNP-based SERS of endocytotic vesicles. However, the induced metabolic changes are subtle. Thus although with the non-functionalised probes SERS active AuNPs inside the 'digestive' endocytotic pathway some differences are identified corresponding to metabolic changes induced by differentiation but distinction of the two cell types was only achieved using the powerful, two-step analysis method of PCA-LDA. PCA alone did not allow for cell group distinction.

### 3.5 Functionalised SERS nanoparticle-probes

Functionalised nanoparticle-probes have been used to target intracellular molecules [76], structures [77] and organelles such as the mitochondria [78], cytoplasm [34] and the cell nucleus [34, 44, 79]. One of the challenges with this approach is to enable the escape of nanoparticles from endocytotic vesicles [30, 77]. Studies have shown that nanoparticle functionalisation achieves cytoplasmic localisation of the cargo using target proteins and peptides such as the cell penetrating peptides (CPPs) [80], SV40 large T antigen [81], HIV-1 Tat peptide [34] as well as adenoviral NLS [44]. Some of these proteins also show nuclear localisation although the majority of internalised particles are still found in endosomes and the cytoplasm [44]. We have used the SV-40 large T nuclear localisation signal bound to 40 nm AuNPs for their successful translocation into the cell nucleus although most of them localise into the cytoplasm as well as endosomes/lysosomes [26]. NLS functionalised AuNPs (NLS-AuNPs) localise into the cytoplasm by escaping the endocytotic pathway and can also translocate into the nucleus as shown in our previous work [26]. Exemplar images of an undifferentiated cell incubated with NLS-AuNPs for 72 h are shown in Figure 5A-C.

In the current work we mainly focussed on AuNPs outside the nucleus. The SERS spectra of UDCs ( $n=16$ ) and DCs ( $n=11$ ) incubated with NLS-AuNPs for 72 hours were characterised using PCA as well as PCA-LDA with regards to their cellular segregation ability as shown in Fig. 5. Single cell PC1 loadings of UDCs (red, top) and DCs (blue, middle) as well as cell group averages (bold blue and red line, bottom) are presented in the top plot in Fig. 5D. PC1 loadings of DCs show a very small divergence. UDCs show a greater divergence, in particular between 1200 and 1600  $\text{cm}^{-1}$  indicating a variation in the amide III band (1200 - 1400  $\text{cm}^{-1}$ ) assigned to proteins. Nevertheless, average PC1 loadings show very distinct shapes allowing for clear cell group segregation. The difference spectrum (black line) in the bottom plot of Fig. 5D reveals shifts in the protein rich regions around 1100 - 1200  $\text{cm}^{-1}$  (peaks at 1160  $\text{cm}^{-1}$  and 1178  $\text{cm}^{-1}$  for DCs and UDCs, respectively) and 1500 - 1700  $\text{cm}^{-1}$  (peaks at 1575  $\text{cm}^{-1}$  and 1585/1605  $\text{cm}^{-1}$  for DCs and UDCs, respectively). Also, there is a change in intensity ratios between various peaks in the PC1 average loadings. Mentioned peaks are assigned to the C-N stretching and the C-H bending in the amino acids tyrosine and phenylalanine [11, 82]. DCs are commonly used as a model of dopaminergic neurons for Parkinson's Disease research [69]. Dopamine beta hydroxylase, an enzyme involved into the synthesis of the neurotransmitters dopamine and norepinephrine, has been shown to be present in DCs [83]. Amino acid peaks found in DCs are also present in spectra of dopamine and norepinephrine [84] suggesting the presence of these neurotransmitters in DCs and their contribution to SERS spectra. To confirm the validity of this hypothesis, UDCs and DCs were fluorescently immune-stained for dopamine and the results are shown in Fig. 6. Besides nuclear staining (Fig. 6A and 6D), fluorescence images for dopamine (Fig. 6B and 6E) and merged images (Fig. 6C and 6D) show the presence of dopamine in some DCs (Fig. 6D-F) in contrast to UDCs (Fig. 6A-C). Overall these differences reflect in the PC1 loadings (Fig. 5D) and allow for distinct cell group segregation.

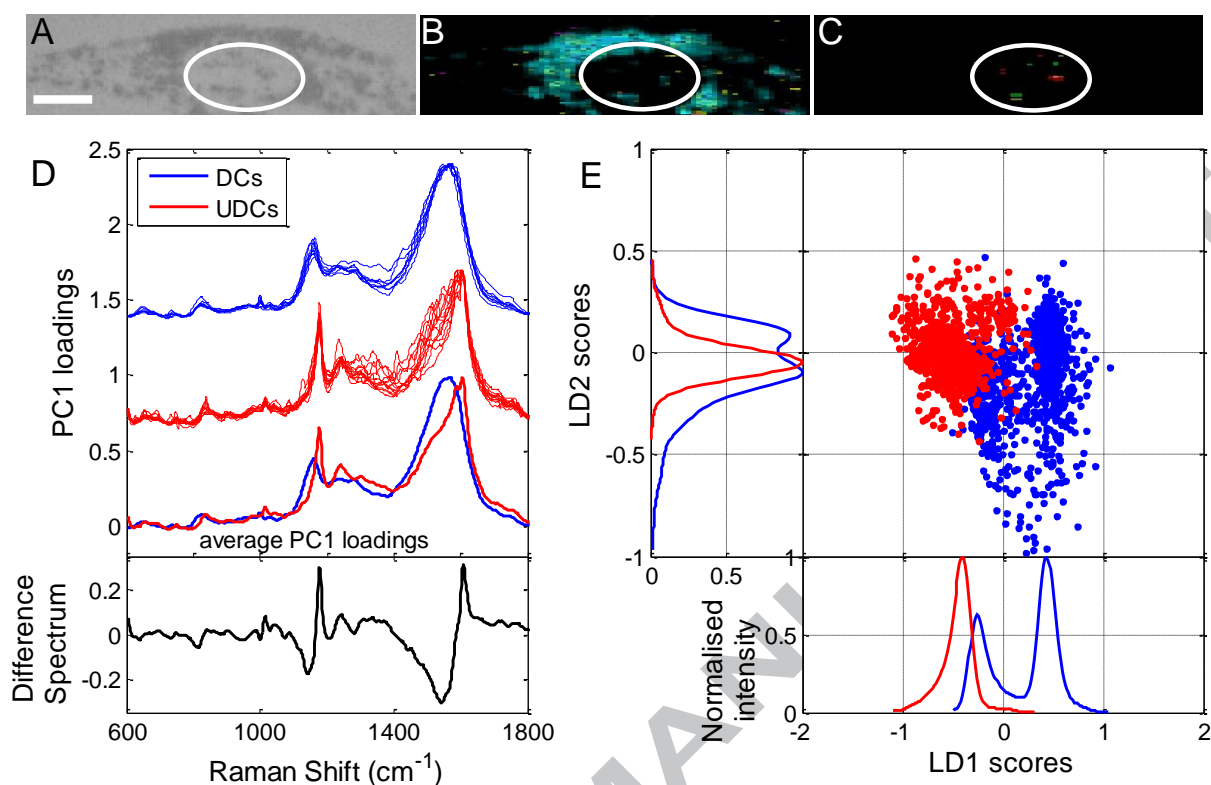


Figure 5: A) Bright field image of a UDC after 72 hours of incubation with 40 nm NLS functionalised AuNPs showing many intracellular particle aggregates outside as well as a few inside the cell nucleus as highlighted with a white ellipse (scale bar: 10  $\mu\text{m}$ ). Corresponding SERS maps (B-C) revealing the intracellular distribution of proteins (B, green: C-C/C-N stretch, yellow: C-H deformation, cyan: C-H<sub>3</sub> deformation) and nucleic acids (C, red: DNA bands at 670, 830, 1375 and 1580 $\text{cm}^{-1}$  and green: RNA peak at 815 $\text{cm}^{-1}$ ). The SERS images were generated by scanning with a pixel size of 600 nm x 600 nm. PCA (D) and PCA-LDA (E) of intracellular NLS-AuNPs in UDCs (red) and DCs (blue). The top figure in (D) shows the PC1 loadings plot for single cells (top for DCs, middle for UDCs) and cell group average (bottom). The difference spectrum (bottom plot in (D)) reveals significant difference between UDCs and DCs in the amino acid regions around 1100 - 1200 $\text{cm}^{-1}$  and 1500 - 1700 $\text{cm}^{-1}$ . Peaks in these region show an amplitude of 20 - 30% compared to the average PC1 loadings. E) LD1 vs. LD2 scatter plot with corresponding 1D intensity curves showing a double peak distribution of LD1 and LD2 scores for DCs with one peak overlaying the distribution of UDCs. This indicates the existence of in common intracellular content as well as molecular dissimilarities allowing for clear cellular distinction.

Further, however, we performed LDA on the PCA results. These are shown in the LD1 vs. LD2 scatter plot and corresponding average 1D intensity curves in Fig. 5E (see Supporting Information for single cell 1D intensity curves of UDCs and DCs). DCs show a double peak distribution for LD1 and LD2 scores peaking at -0.26/0.44 and -0.09/0.09, respectively. For UDCs, LD1 and LD2 scores show an almost Gaussian-shaped curve with slight negative skew for LD1 and slight positive skew for LD2. They peak at -0.40 and 0.05 for LD1 and LD2 scores, respectively. Functionalisation of AuNPs results in a smaller overlap of LD1/LD2 scores of both cell groups. Negative LD1 scores of DCs overlap with UDCs suggesting the common molecular features of these cell groups. However, the majority of the data points of the LD1 scores of DCs reveal positive values and are free of overlap with UDCs demonstrating the presence of significant, molecular dissimilarities. Therefore, LD1 scores allow for complete cell group classification.

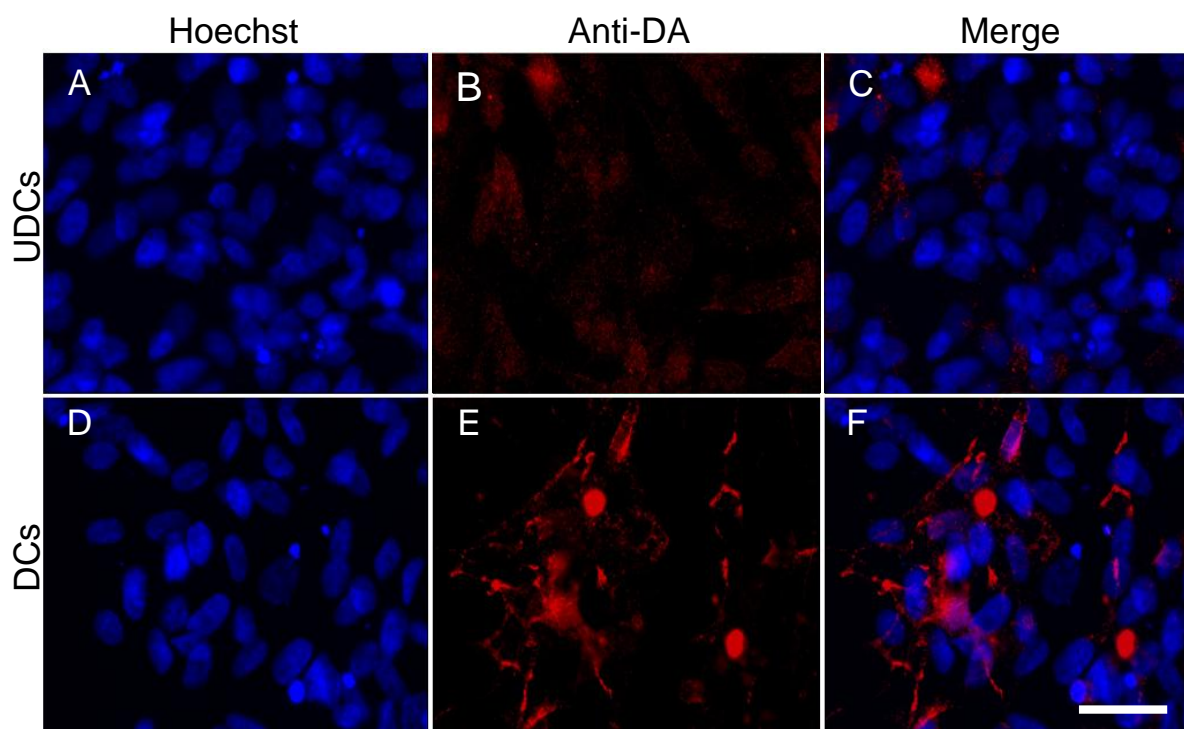


Figure 6: Hoechst 33342 (A, D) / Anti-dopamine antibody (B, E) double staining of UDCs (top row) and DCs (bottom row) for visualisation of the intracellular dopamine distribution. Merged fluorescence image of UDCs (C) shows only fluorescence background, in contrast to that of DCs (F) which proves the presence of intracellular dopamine.

Comparing these results to intracellular SERS of non-functionalised AuNPs, an enormous improvement in group classification was achieved by considering spectra from outside the nuclear region (the cytoplasm in addition to those from endosomes/lysosomes). Not only a very clear segregation could be accomplished using PCA-LDA but also potential intracellular changes induced by cell differentiation were visualised using PC1 loadings with functionalised AuNPs.

#### 4. Conclusion

In this study, we have investigated the uptake of AuNPs and their use as suitable nanoparticle-sensors for intracellular SERS imaging. Taken up and after being processed through the endocytotic pathways (endosomes/lysosomes), their motility within this pathway was investigated using particle tracking and revealed the intracellular diffusion coefficients as well as characteristic transport velocities of endocytotic vesicles. Understanding NP uptake is of great relevance to intracellular SERS and allows probing the 'digestive' system of the cell. Insight into metabolic and intracellular dissimilarities of different cell (pheno)types was gained by studying SERS signals from the cytoplasm and the endocytotic vesicles. Intracellular SERS allowed for segregation of closely related cell phenotypes using a combination of principle component and linear discriminant analysis although functionalised AuNPs were found to be better than non-functionalised AuNPs. In comparison to UDCs, DCs showed a significant presence of specific amino acids involved in the synthesis of neurotransmitters such as dopamine and norephenepine suggesting dopamine beta hydroxylase activity. Furthermore, PC loadings as well as PCA-LDA allowed for clear phenotype distinction. This work therefore highlights that AuNPs based SERS imaging could be of great importance for

biomedical research involving molecular characterisation and intracellular imaging of different cell types.

## References

1. Boisselier, E. and Astruc, D., 'Gold Nanoparticles in Nanomedicine: Preparations, Imaging, Diagnostics, Therapies and Toxicity', *Chem Soc Rev*, 2009, 38, (6), pp. 1759-1782.
2. Sailor, M.J. and Park, J.-H., 'Hybrid Nanoparticles for Detection and Treatment of Cancer', *Adv Mater*, 2012, 24, (28), pp. 3779-3802.
3. Suh, J., Dawson, M., and Hanes, J., 'Real-Time Multiple-Particle Tracking: Applications to Drug and Gene Delivery', *Adv Drug Deliver Rev*, 2005, 57, (1), pp. 63-78.
4. Schlücker, S., 'Sers Microscopy: Nanoparticle Probes and Biomedical Applications', *ChemPhysChem*, 2009, 10, (9-10), pp. 1344-1354.
5. Nie and Emory, 'Probing Single Molecules and Single Nanoparticles by Surface-Enhanced Raman Scattering', *Science*, 1997, 275, (5303), pp. 1102-1106.
6. Hossain, M.K. and Yukihiko, A.O., 'Surface-Enhanced Raman Scattering Facts and Inline Trends', *Curr Sci India*, 2009, 97, (2), pp. 192-201.
7. Campion, A. and Kambhampati, P., 'Surface-Enhanced Raman Scattering', *Chem Soc Rev*, 1998, 27, (4), pp. 241-250.
8. Schwartzberg, A.M., Grant, C.D., Wolcott, A., Talley, C.E., Huser, T.R., Bogomolni, R., and Zhang, J.Z., 'Unique Gold Nanoparticle Aggregates as a Highly Active Surface-Enhanced Raman Scattering Substrate', *J Phys Chem B*, 2004, 108, (50), pp. 19191-19197.
9. Kneipp, J., Kneipp, H., Wittig, B., and Kneipp, K., 'Novel Optical Nanosensors for Probing and Imaging Live Cells', *NanoMed-Nanotechnol*, 2010, 6, (2), pp. 214-226.
10. Mahajan, S., Richardson, J., Brown, T., and Bartlett, P.N., 'Sers-Melting: A New Method for Discriminating Mutations in DNA Sequences', *J Am Chem Soc*, 2008, 130, (46), pp. 15589-15601.
11. Kneipp, J., Kneipp, H., McLaughlin, M., Brown, D., and Kneipp, K., 'In Vivo Molecular Probing of Cellular Compartments with Gold Nanoparticles and Nanoaggregates', *Nano Lett*, 2006, 6, (10), pp. 2225-2231.
12. Li, L., Hutter, T., Steiner, U., and Mahajan, S., 'Single Molecule Sers and Detection of Biomolecules with a Single Gold Nanoparticle on a Mirror Junction', *Analyst*, 2013, 138, (16), pp. 4574-4578.
13. Faulds, K., Smith, W.E., Graham, D., and Lacey, R.J., 'Assessment of Silver and Gold Substrates for the Detection of Amphetamine Sulfate by Surface Enhanced Raman Scattering (Sers)', *Analyst*, 2002, 127, (2), pp. 282-286.
14. Samanta, A., Maiti, K.K., Soh, K.-S., Liao, X., Vendrell, M., Dinish, U.S., Yun, S.-W., Bhuvanewari, R., Kim, H., Rautela, S., Chung, J., Olivo, M., and Chang, Y.-T., 'Ultrasensitive near-Infrared Raman Reporters for Sers-Based in Vivo Cancer Detection', *Angew. Chem. Int. Ed.*, 2011, 50, (27), pp. 6089-6092.
15. Li, X., Yang, T., and Lin, J., 'Spectral Analysis of Human Saliva for Detection of Lung Cancer Using Surface-Enhanced Raman Spectroscopy', *J Biomed Opt*, 2012, 17, (3), pp. 037003-037005.
16. Feng, S., Lin, J., Huang, Z., Chen, G., Chen, W., Wang, Y., Chen, R., and Zeng, H., 'Esophageal Cancer Detection Based on Tissue Surface-Enhanced Raman Spectroscopy and Multivariate Analysis', *Appl Phys Lett*, 2013, 102, (4), pp. 043702-043702-043704.
17. Kim, J.A., Åberg, C., Salvati, A., and Dawson, K.A., 'Role of Cell Cycle on the Cellular Uptake and Dilution of Nanoparticles in a Cell Population', *Nat Nanotechnol*, 2012, 7, (1), pp. 62-68.
18. Abalde-Cela, S., Aldeanueva-Potel, P., Mateo-Mateo, C., Rodríguez-Lorenzo, L., Alvarez-Puebla, R., Ocaña, A., Liz-Marzán, J. J., and Liz-Marzán, L.M., 'Surface-Enhanced Raman Scattering Biomedical Applications of Plasmonic Colloidal Particles', *J R Soc Interfac*, 2010, 7 Suppl 4, pp. S435-450.

19. Kneipp, K., Kneipp, H., Itzkan, I., Dasari, R.R., and Feld, M.S., 'Surface-Enhanced Raman Scattering and Biophysics', *J Phys.: Condens Matter*, 2002, 14, (18), p. R597.
20. Escoriza, M.F., VanBriesen, J.M., Stewart, S., and Maier, J., 'Raman Spectroscopic Discrimination of Cell Response to Chemical and Physical Inactivation', *Appl Spectrosc*, 2007, 61, (8), pp. 812-823.
21. Kang, J. and Gu, H., 'Probing of Cancer Cell Apoptosis by Sers and Lscm', in Amzajerian, F., Gao, C.-q., and Xie, T.-y. (eds.), (SPIE, 2009, 1 edn.)
22. Xie, W., Wang, L., Zhang, Y., Su, L., Shen, A., Tan, J., and Hu, J., 'Nuclear Targeted Nanoprobe for Single Living Cell Detection by Surface-Enhanced Raman Scattering', *Bioconjugate Chem*, 2009, 20, (4), pp. 768-773.
23. Kneipp, K., Haka, A.S., Kneipp, H., Badizadegan, K., Yoshizawa, N., Boone, C., Shafer-Peltoer, K.E., Motz, J.T., Dasari, R.R., and Feld, M.S., 'Surface-Enhanced Raman Spectroscopy in Single Living Cells Using Gold Nanoparticles', *Appl Spectrosc*, 2002, 56, (2), p. 5.
24. Ock, K., Jeon, W.I., Ganbold, E.O., Kim, M., Park, J., Seo, J.H., Cho, K., Joo, S.-W., and Lee, S.Y., 'Real-Time Monitoring of Glutathione-Triggered Thiopurine Anticancer Drug Release in Live Cells Investigated by Surface-Enhanced Raman Scattering', *Anal. Chem.*, 2012, 84, (5), pp. 2172-2178.
25. Matthäus, C., Chernenko, T., Newmark, J.A., Warner, C.M., and Diem, M., 'Label-Free Detection of Mitochondrial Distribution in Cells by Nonresonant Raman Microspectroscopy', *Biophys J*, 2007, 93, (2), pp. 668-673.
26. Huefner, A., Kuan, W.-L., Barker, R.A., and Mahajan, S., 'Intracellular Sers Nanoprobes for Distinction of Different Neuronal Cell Types', *Nano Lett*, 2013.
27. Candeloro, P., Tirinato, L., Malara, N., Fregola, A., Casals, E., Puntès, V., Perozziello, G., Gentile, F., Coluccio, M.L., Das, G., Liberale, C., De Angelis, F., and Di Fabrizio, E., 'Nanoparticle Microinjection and Raman Spectroscopy as Tools for Nanotoxicology Studies', *Analyst*, 2011, 136, (21), pp. 4402-4408.
28. Feldherr, C.M. and Akin, D., 'The Permeability of the Nuclear Envelope in Dividing and Nondividing Cell Cultures', *J Cell Biol*, 1990, 111, (1), pp. 1-8.
29. Lin, J., Chen, R., Feng, S., Li, Y., Huang, Z., Xie, S., Yu, Y., Cheng, M., and Zeng, H., 'Rapid Delivery of Silver Nanoparticles into Living Cells by Electroporation for Surface-Enhanced Raman Spectroscopy', *Biosens Bioelectron*, 2009, 25, (2), pp. 388-394.
30. Lévy, R., Shaheen, U., Cesbron, Y., and Sée, V., 'Gold Nanoparticle Delivery in Mammalian Live Cells: A Critical Review', *Nano Reviews*, 2010, 1, p. 4889.
31. Klein, T.M., Wolf, E.D., Wu, R., and Sanford, J.C., 'High-Velocity Microprojectiles for Delivering Nucleic Acids into Living Cells', *Nature*, 1987, 327, (6117), pp. 70-73.
32. Liang, W. and Lam, J.K.W., *Endosomal Escape Pathways for Non-Viral Nucleic Acid Delivery Systems*, (InTech, 2012)
33. Verma, A. and Stellacci, F., 'Effect of Surface Properties on Nanoparticle-Cell Interactions', *Small*, 2010, 6, (1), pp. 12-21.
34. de la Fuente, J.M. and Berry, C.C., 'Tat Peptide as an Efficient Molecule to Translocate Gold Nanoparticles into the Cell Nucleus', *Bioconjugate Chem*, 2005, 16, (5), pp. 1176-1180.
35. Zhang, S., Li, J., Lykotrafitis, G., Bao, G., and Suresh, S., 'Size-Dependent Endocytosis of Nanoparticles', *Adv Mater*, 2009, 21, (4), pp. 419-424.
36. Cho, E.C., Zhang, Q., and Xia, Y., 'The Effect of Sedimentation and Diffusion on Cellular Uptake of Gold Nanoparticles', *Nat Nano*, 2011, 6, (6), pp. 385-391.
37. Tkachenko, A.G., Xie, H., Liu, Y., Coleman, D., Ryan, J., Glomm, W.R., Shipton, M.K., Franzen, S., and Feldheim, D.L., 'Cellular Trajectories of Peptide-Modified Gold Particle Complexes: Comparison of Nuclear Localization Signals and Peptide Transduction Domains', *Bioconjugate Chem*, 2004, 15, (3), pp. 482-490.
38. Lynch, I., Cedervall, T., Lundqvist, M., Cabaleiro-Lago, C., Linse, S., and Dawson, K.A., 'The Nanoparticle-Protein Complex as a Biological Entity; a Complex Fluids and Surface Science Challenge for the 21st Century', *Adv Colloid Interfac*, 2007, 134-135, (0), pp. 167-174.

39. Albanese, A., Tang, P.S., and Chan, W.C.W., 'The Effect of Nanoparticle Size, Shape, and Surface Chemistry on Biological Systems', *Annu Rev Biomed Eng*, 2012, 14, (1), pp. 1-16.
40. Mironava, T., Hadjiargyrou, M., Simon, M., Jurukovski, V., and Rafailovich, M.H., 'Gold Nanoparticles Cellular Toxicity and Recovery: Effect of Size, Concentration and Exposure Time', *Nanotoxicology*, 2010, 4, (1), pp. 120-137.
41. Panariti, A., Misericocchi, G., and Rivolta, I., 'The Effect of Nanoparticle Uptake on Cellular Behavior: Disrupting or Enabling Functions?', *Nanotechnology, Science and Applications*, 2012, 2012:5, pp. 87-100.
42. McMahon, H.T. and Boucrot, E., 'Molecular Mechanism and Physiological Functions of Clathrin-Mediated Endocytosis', *Nat Rev Mol Cell Bio*, 2011, 12, (8), pp. 517-533.
43. Albanese, A. and Chan, W.C.W., 'Effect of Gold Nanoparticle Aggregation on Cell Uptake and Toxicity', *ACS nano*, 2011, 5, (7), pp. 5478-5489.
44. Tkachenko, A.G., Xie, H., Coleman, D., Glomm, W., Ryan, J., Anderson, M.F., Franzen, S., and Feldheim, D.L., 'Multifunctional Gold Nanoparticle-Peptide Complexes for Nuclear Targeting', *J Am Chem Soc*, 2003, 125, (16), pp. 4700-4701.
45. Vale, R.D., 'The Molecular Motor Toolbox for Intracellular Transport', *Cell*, 2003, 112, (4), pp. 467-480.
46. Cai, D., Verhey, K.J., and Meyhöfer, E., 'Tracking Single Kinesin Molecules in the Cytoplasm of Mammalian Cells', *Biophys J*, 2007, 92, (12), pp. 4137-4144.
47. Friedman, D.S. and Vale, R.D., 'Single-Molecule Analysis of Kinesin Motility Reveals Regulation by the Cargo-Binding Tail Domain', *Nat Cell Biol*, 1999, 1, (5), pp. 293-297.
48. Courty, S., Luccardini, C., Bellaiche, Y., Cappello, G., and Dahan, M., 'Tracking Individual Kinesin Motors in Living Cells Using Single Quantum-Dot Imaging', *Nano Lett*, 2006, 6, (7), pp. 1491-1495.
49. Levi, V. and Gratton, E., 'Exploring Dynamics in Living Cells by Tracking Single Particles', *Cell Biochem Biophys*, 2007, 48, (1), pp. 1-15.
50. Levi, V., Ruan, Q., and Gratton, E., '3-D Particle Tracking in a Two-Photon Microscope: Application to the Study of Molecular Dynamics in Cells', *Biophys J*, 2005, 88, (4), pp. 2919-2928.
51. Caspi, A., Yeger, O., Grosheva, I., Bershady, A.D., and Elbaum, M., 'A New Dimension in Retrograde Flow: Centripetal Movement of Engulfed Particles', *Biophys J*, 2001, 81, (4), pp. 1990-2000.
52. Toshima, J.Y., Toshima, J., Kaksonen, M., Martin, A.C., King, D.S., and Drubin, D.G., 'Spatial Dynamics of Receptor-Mediated Endocytic Trafficking in Budding Yeast Revealed by Using Fluorescent A-Factor Derivatives', *P. Natl. Acad. Sci. USA*, 2006, 103, (15), pp. 5793-5798.
53. Bálint, Š., Verdeny Vilanova, I., Sandoval Álvarez, Á., and Lakadamyali, M., 'Correlative Live-Cell and Superresolution Microscopy Reveals Cargo Transport Dynamics at Microtubule Intersections', *P Natl Acad Sci USA*, 2013, 110, (9), pp. 3375-3380.
54. Kuan, W.-L., Poole, E., Fletcher, M., Karniely, S., Tyers, P., Wills, M., Barker, R.A., and Sinclair, J.H., 'A Novel Neuroprotective Therapy for Parkinson's Disease Using a Viral Noncoding Rna That Protects Mitochondrial Complex I Activity', *The Journal of Experimental Medicine*, 2012, 209, (1), pp. 1-10.
55. Schneider, C.A., Rasband, W.S., and Eliceiri, K.W., 'Nih Image to ImageJ: 25 Years of Image Analysis', *Nat Meth*, 2012, 9, (7), pp. 671-675.
56. Smith, Matthew B., Karatekin, E., Gohlke, A., Mizuno, H., Watanabe, N., and Vavylonis, D., 'Interactive, Computer-Assisted Tracking of Speckle Trajectories in Fluorescence Microscopy: Application to Actin Polymerization and Membrane Fusion', *Biophys J*, 2011, 101, (7), pp. 1794-1804.
57. Chanana, M., Rivera\_Gil, P., Correa-Duarte, M.A., Liz-Marzán, L.M., and Parak, W.J., 'Physicochemical Properties of Protein-Coated Gold Nanoparticles in Biological Fluids and Cells before and after Proteolytic Digestion', *Angew Chem Int Ed*, 2013, 52, (15), pp. 4179-4183.

58. Trevisan, J., Angelov, P.P., Scott, A.D., Carmichael, P.L., and Martin, F.L., 'Irootlab: A Free and Open-Source Matlab Toolbox for Vibrational Biospectroscopy Data Analysis', *Bioinformatics*, 2013, 29, (8), pp. 1095-1097.
59. Martin, F.L., Kelly, J.G., Llabjani, V., Martin-Hirsch, P.L., Patel, I.I., Trevisan, J., Fullwood, N.J., and Walsh, M.J., 'Distinguishing Cell Types or Populations Based on the Computational Analysis of Their Infrared Spectra', *Nat. Protocols*, 2010, 5, (11), pp. 1748-1760.
60. Yang, J. and Yang, J.-y., 'Why Can Lda Be Performed in Pca Transformed Space?', *Lect. Notes Comput. Sc.*, 2003, 36, (2), pp. 563-566.
61. Chithrani, B.D., Ghazani, A.A., and Chan, W.C.W., 'Determining the Size and Shape Dependence of Gold Nanoparticle Uptake into Mammalian Cells', *Nano Lett*, 2006, 6, (4), pp. 662-668.
62. Lu, F., Wu, S.-H., Hung, Y., and Mou, C.-Y., 'Size Effect on Cell Uptake in Well-Suspended, Uniform Mesoporous Silica Nanoparticles', *Small*, 2009, 5, (12), pp. 1408-1413.
63. Chithrani, D.B., 'Intracellular Uptake, Transport, and Processing of Gold Nanostructures', *Mol Membr Biol*, 2010, 27, (7), pp. 299-311.
64. Ross, J.L., Ali, M.Y., and Warshaw, D.M., 'Cargo Transport: Molecular Motors Navigate a Complex Cytoskeleton', *Current Opinion in Cell Biology*, 2008, 20, (1), pp. 41-47.
65. Jin, H., Heller, D.A., and Strano, M.S., 'Single-Particle Tracking of Endocytosis and Exocytosis of Single-Walled Carbon Nanotubes in Nih-3t3 Cells', *Nano Lett*, 2008, 8, (6), pp. 1577-1585.
66. Tsuji, T., Kawai-Noma, S., Pack, C.-G., Terajima, H., Yajima, J., Nishizaka, T., Kinjo, M., and Taguchi, H., 'Single-Particle Tracking of Quantum Dot-Conjugated Prion Proteins inside Yeast Cells', *Biochem Bioph Res Co*, 2011, 405, (4), pp. 638-643.
67. Coppin, C.M., Pierce, D.W., Hsu, L., and Vale, R.D., 'The Load Dependence of Kinesin's Mechanical Cycle', *P Natl Acad Sci USA*, 1997, 94, (16), pp. 8539-8544.
68. Wu, H., Volponi, J.V., Oliver, A.E., Parikh, A.N., Simmons, B.A., and Singh, S., 'In Vivo Lipidomics Using Single-Cell Raman Spectroscopy', *P Natl Acad Sci USA*, 2011, 108, (9), pp. 3809-3814.
69. Xie, H., Hu, L., and Li, G., 'Sh-Sy5y Human Neuroblastoma Cell Line: In Vitro Cell Model of Dopaminergic Neurons in Parkinson's Disease', *Chin Med J (Engl)*, 2010, 123, (8), pp. 1086-1092.
70. Bruno, S., Ardelt, B., Skierski, J.S., Traganos, F., and Darzynkiewicz, Z., 'Different Effects of Staurosporine, an Inhibitor of Protein Kinases, on the Cell Cycle and Chromatin Structure of Normal and Leukemic Lymphocytes', *Cancer Res*, 1992, 52, (2), pp. 470-473.
71. Stanwell, C., Dlugosz, A.A., and Yuspa, S.H., 'Staurosporine Induces a Complete Program of Terminal Differentiation in Neoplastic Mouse Keratinocytes Via Activation of Protein Kinase C', *Carcinogenesis*, 1996, 17, (6), pp. 1259-1265.
72. Deshmukh, M. and Johnson, E.M., 'Staurosporine-Induced Neuronal Death: Multiple Mechanisms and Methodological Implications', *Cell Death Differ*, 2000, 7, (3).
73. Zhou, W., Choi, M., Margineantu, D., Margaretha, L., Hesson, J., Cavanaugh, C., Blau, C.A., Horwitz, M.S., Hockenbery, D., Ware, C., and Ruohola-Baker, H., 'Hif1[Alpha] Induced Switch from Bivalent to Exclusively Glycolytic Metabolism During Esc-to-Episc/Hesc Transition', *EMBO J*, 2012, 31, (9), pp. 2103-2116.
74. McGraw, T.E. and Mittal, V., 'Stem Cells: Metabolism Regulates Differentiation', *Nat Chem Biol*, 2010, 6, (3), pp. 176-177.
75. Zhang, J., Nuebel, E., Daley, George Q., Koehler, Carla M., and Teitell, Michael A., 'Metabolic Regulation in Pluripotent Stem Cells During Reprogramming and Self-Renewal', *Cell Stem Cell*, 2012, 11, (5), pp. 589-595.
76. Schlücker, S., Küstner, B., Punge, A., Bonfig, R., Marx, A., and Ströbel, P., 'Immuno-Raman Microspectroscopy: In Situ Detection of Antigens in Tissue Specimens by Surface-Enhanced Raman Scattering', *J Raman Spectrosc*, 2006, 37, (7), pp. 719-721.
77. Huang, J.G., Leshuk, T., and Gu, F.X., 'Emerging Nanomaterials for Targeting Subcellular Organelles', *Nano Today*, 2011, 6, (5), pp. 478-492.

78. Yamada, Y., Akita, H., Kamiya, H., Kogure, K., Yamamoto, T., Shinohara, Y., Yamashita, K., Kobayashi, H., Kikuchi, H., and Harashima, H., 'Mito-Porter: A Liposome-Based Carrier System for Delivery of Macromolecules into Mitochondria Via Membrane Fusion', *BBA-Biomembranes*, 2008, 1778, (2), pp. 423-432.
79. Kang, B., Mackey, M.A., and El-Sayed, M.A., 'Nuclear Targeting of Gold Nanoparticles in Cancer Cells Induces DNA Damage, Causing Cytokinesis Arrest and Apoptosis', *J Am Chem Soc*, 2010, 132, (5), pp. 1517-1519.
80. Nativo, P., Prior, I.A., and Brust, M., 'Uptake and Intracellular Fate of Surface-Modified Gold Nanoparticles', *ACS nano*, 2008, 2, (8), pp. 1639-1644.
81. Ryan, J.A., Overton, K.W., Speight, M.E., Oldenburg, C.N., Loo, L., Robarge, W., Franzen, S., and Feldheim, D.L., 'Cellular Uptake of Gold Nanoparticles Passivated with Bsa-Sv40 Large T Antigen Conjugates', *Anal Chem*, 2007, 79, (23), pp. 9150-9159.
82. Boyd, A., McManus, L., Burke, G., and Meenan, B., 'Raman Spectroscopy of Primary Bovine Aortic Endothelial Cells: A Comparison of Single Cell and Cell Cluster Analysis', *J Mater Sci-Mater M*, 2011, 22, (8), pp. 1923-1930.
83. Oyarce, A.M. and Fleming, P.J., 'Multiple Forms of Human Dopamine Beta-Hydroxylase in Sh-Sy5y Neuroblastoma Cells', *Archives of biochemistry and biophysics*, 1991, 290, (2), pp. 503-510.
84. Lee, N.S., Hsieh, Y.Z., Paisley, R.F., and Morris, M.D., 'Surface-Enhanced Raman Spectroscopy of the Catecholamine Neurotransmitters and Related Compounds', *Anal Chem*, 1988, 60, (5), pp. 442-446.